THE JOURNAL OF PHYSICAL CHEMISTRY A

Article

Cite This: J. Phys. Chem. A 2019, 123, 2080−2090

pubs.acs.org/JPCA

Investigation of Conversion and Decay Processes in Thermally Activated Delayed Fluorescence Copper(I) Molecular Crystal: Theoretical Estimations from an ONIOM Approach Combined with the Tuned Range-Separated Density Functional Theory

Lingling Lv,*[,†,‡] Kun Yuan,[†,‡] Yuancheng Zhu,[†,‡] Guofang Zuo,[†] and Yongcheng Wang[§]

[†]College of Chemical Engineering and Technology, Tianshui Normal University, Tianshui, Gansu 741001, China

[‡]Supercomputing Center for Theoretical Chemistry, Tianshui Normal University, Tianshui, GanSu 741001, China

[§]College of Chemistry and Chemical Engineering, Northwest Normal University, Lanzhou, Gansu 730070, China

Supporting Information

ABSTRACT: Accurate research of the photophysical processes is of great significance for the rational design of excellent thermally activated delayed fluorescence (TADF) materials. Herein, the interconversion and decay rates of the first excited singlet state (S_1) and triplet states (T_1) in the Cu(pop)(pz_2BH_2) complex are computed using the thermal vibration correlation function (TVCF) theory at different temperature. For consideration of the solid-state environment, a methodology that is based on the ONIOM model, combined with the optimally tuned range-separated hybrid functional (CAM-B3LYP*) method, was applied. Our calculated results are in excellent agreement with the experimentally available data. It has been found that the energy dissipation of the nonradiative processes from the S_1 to ground state is promoted by low frequency vibrational modes in the solution phase, resulting in the high $k_{nr}(S) = 1.68 \times 10^8\ s^{-1}$ at 300 K. However, for the crystal phase, they are easily hindered through intermolecular interactions, $k_{nr}(S)$ is predicted to be decreased by about 5 orders of magnitude upon aggregation ($2.98 \times 10^3\ s^{-1}$). With temperature increase, the reverse intersystem crossing (RISC) rate k_{RISC} from T_1 to S_1 is drastically increased to $6.12 \times 10^4\ s^{-1}$ at 300 K, while the change of other rates is still small, which can compete with the radiative decay rate of $k_r(T) = 4.75 \times 10^4\ s^{-1}$ and nonradiative intersystem crossing rate of $k_{ISC}(T_1-S_0) = 6.63 \times 10^2\ s^{-1}$ at the T_1 state. This implies that the S_1 state can be an efficient thermal population from the T_1 state, leading to an occurrence of delayed fluorescence, and the complexes exhibit high emission quantum yields, 58.7%. But, at low temperature $T < 100$ K, the RISC rate is sharply change, $k_{RISC} \ll k_r(T)$ or k_{ISC}, which cannot induce an occurrence of delayed fluorescence. Our investigation would be helpful for designing novel, high-efficiency TADF materials.

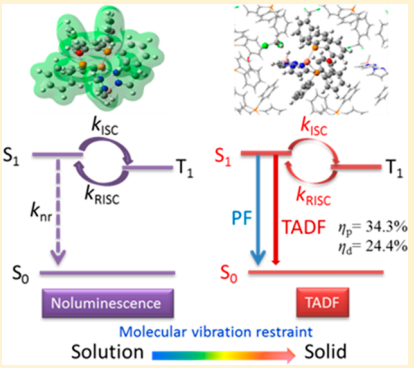

1. INTRODUCTION

Organic light emitting diodes (OLEDs) have been investigated for about 2 decades now and undergone developments of three generations.[1−3] One key advantage of the third-generation emitters is a recycling of excitons between the singlet (S_1) and triplet manifolds ($T_{0,\pm1}$) with a rather small singlet−triplet energy gap $\Delta E(S_1-T_1)$ via reverse intersystem crossing (RISC) with the help of thermal energy at room temperature.[4] This luminescence is so-called the thermally activated delayed fluorescence (TADF), which gives rise to the theoretical maximum quantum yield from 25% for the first-generation fluorescent emitters to 100%.[5,6] Another advantage is that TADF emitters do not include expensive and possibly toxic heavy metals as compared to the second-generation phosphorescent emitters.

Cu(I) complexes as a new generation with TADF emitters have come to the attention of the academic and commercial communities.[7] Some of their derivatives show excellent TADF phenomena and extremely high photoluminescence quantum yield in the solid phase,[8−10] and are also found to display extensive strong emitters in the solid phase, with the so-called "aggregation-induced emission (AIE)" features.[11,12] However, it is well-established that most TADF emitters suffer from aggregation-caused quenching in the condensed phase, which restrains the efficiency enhancement of OLEDs. Effective TADF molecules have to be dispersed into host matrices only with careful control of their concentration to suppress exciton annihilation and aggregation quenching, which usually becomes a baffle to device stability and practical application. Coexistence of TADF and AIE in emitters is an excellent strategy to solve this problem. AIE molecules were first reported by Tang et al.,[13] and they usually show weak emission

Received: January 11, 2019
Revised: February 20, 2019
Published: February 25, 2019

DOI: 10.1021/acs.jpca.9b00321
J. Phys. Chem. A 2019, 123, 2080−2090

or no radiation in dilute solution but become strong emitters in a rigid environment (such as a solid film). AIE and TADF coexistence in two new Cu(I) compounds has been reported by Bryce et al.[14]

Recently, H. Yersin et al.[12] experimentally reported that the Cu(pop)(pz_2BH_2) complex, with pop = bis(2-(diphenylphosphanyl)-phenyl)ether and pz_2BH_2 = bis(pyrazol-1-yl)-borohydrate (Figure 1) is poorly luminescent in CH_2Cl_2 at

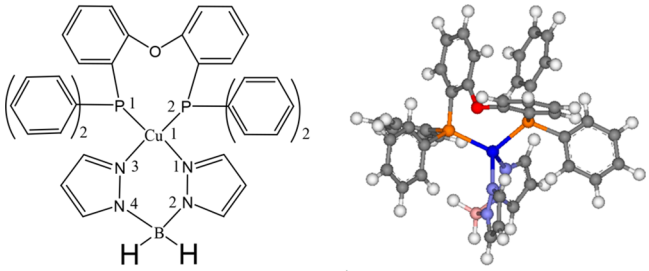

Figure 1. Chemical structure of mononuclear Cu(pop)(pz_2BH_2) complex.

room temperature, with a fluorescence quantum yield Φ_p as low as 9%. However, the emission efficiency in the thin film phase or powder increases to 35% and 45%, respectively, namely increased by 4−5 times. In contrast to experimental researches, so far theoretical efforts on comprehensive understanding of emission properties seem to be quite scarce, in particular, the influence of the environment onto the TADF-AIE mechanism.[14−16]

It is well-known that theoretical simulation not only provides a much deeper understanding of photophysical properties of the Cu(I) complexes but also provides some modern ideas for the development of an enormous number of new materials. But, a reliable and efficient simulation method for the prediction of the excited state properties is prerequisites for theoretical calculations, as it would allow one to possibly help in determining the origin of variation in experimental results. Currently, it is a large challenge to be able to describe accurately the solid phase charge transfer (CT) excited-state properties of TADF emitters in theoretical studies.[17,18] Certainly, time-dependent density functional theory (TD-DFT) is the most widely used method for theoretical interpretation of the excited state properties of relatively larger systems. However, one key issue is that TD-DFT calculations according to default standard functionals can fail completely in predicting of the electronic structure for TADF molecules with CT characteristics, these systematic errors mainly originated from the introduction of inappropriate exchange-correlation (XC) approximations, and can be further lead to delocalization error, lack of derivative discontinuity, as well as wrong asymptotic behaviors of large distance.[17] Therefore, the mixing of an appropriate, certain amount of exact-exchange (eX) functional has been demonstrated to provide excellent description of the properties of charge transfer excited states. In addition, the previous works indicate that some amount of short-range HF exchange (that is to set α to a nonzero value), can also further improve electronic properties and excitation energies.[19−21] Therefore, in this study, we choose a range-separated, coulomb-attenuating method, CAM-B3LYP (α = 0.19; $\alpha + \beta$ = 0.65; short-range to long-range: 19% to 65%) in combination with tuning ω (range-separation parameter) in solution and solid phases via the nonempirical procedure, which is denoted as CAM-B3LYP*.

Another important issue in the computational model of TADF that has received little attention is the description of solid environmental effects. To better study the behaviors of the AIE in TADF materials, the solid state environment must be considered. A more computationally efficient method proposed by Sunet al.[22] is where the crystal molecule was "dissolved" in the same solvent as the solute crystal molecules for the simulation of the solid state environment, which is achieved with the help of combining the polarizable continuum model (PCM) with optimally tuned range-separation functionals. The advantage of this method is that it is more accurate in the energy prediction of the CT excited states, but it performs poorly in the geometric optimization. Motivated by the above questions, in this paper, we investigated the aggregation effects on the excited state decays of the TADF-AIE molecules by using a popular quantum mechanics and molecular mechanics (ONIOM) approach[23] combined with a thermal vibration correlation function (TVCF) theory developed by Shuai's group,[24] which provides a quantitative understanding of the aggregation effects.

2. COMPUTATION DETAILS

2.1. Model Setup. The simulation of the crystal phase of the Cu(pop)(pz_2BH_2) molecule is calculated by the QM/MM approach (that is, two-layer ONIOM method). The computational model is constructed according to the X-ray crystal structure, and the detail packing structure (3 × 3 × 3

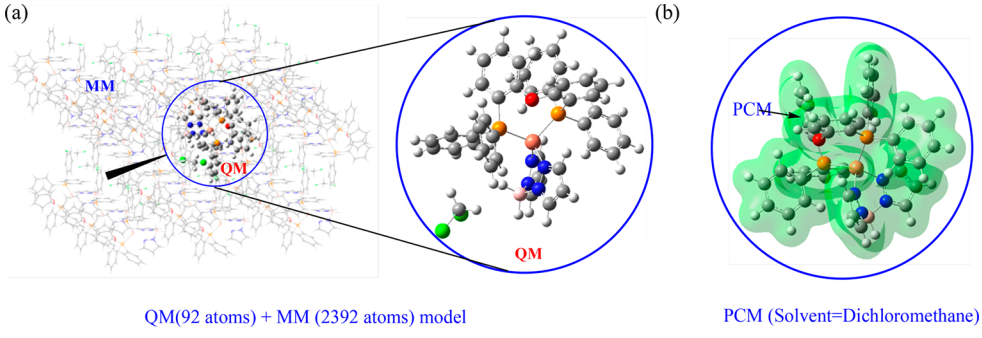

Figure 2. Illustrative picture for constructing the ONIOM QM/MM model of crystal Cu(pop)(pz_2BH_2) (a). For ONIOM QM/MM model: Using a two-level ONIOM model, the centered Cu(pop)(pz_2BH_2)(CH_2Cl_2) is treated as high layer with QM mechanism; its 26 nearest molecules (total 2392 atoms) are regarded as low layer at the MM level. (b) Setup PCM (solvent = CH_2Cl_2) model.

DOI: 10.1021/acs.jpca.9b00321
J. Phys. Chem. A 2019, 123, 2080−2090

supercell) is shown in Figure 2. In the ONIOM calculations, the central molecule having 92 atoms is treated by using the accurate high-level QM method, while the surrounding 26 molecules (2392 atoms) are treated as MM section and are defined as the low-layer. The MM calculation is treated using the efficient universal force field (UFF) method, and the outermost MM part is frozen during the QM/MM geometry optimizations for the S_0, S_1, and T_1 states. In addition, the MM charges are calculated using the QEQ method that is embedded onto the QM calculations to consider the polarization interaction of the MM charges on the QM atoms.

The solvent effects are imitated using PCM. For PCM, solvent (=CH_2Cl_2) is indicated as a homogeneous dielectric medium surrounding the solute Cu(pop)(pz_2BH_2) molecule that is place in a cavity built as envelop of spheres centered on the atomic positions, which is represented as the QM/PCM. In the computation of absorption and emission energies with PCM method, two approaches including state specific (SS) and linear responses (LR) approaches are employed in this paper. In the former, the solvent reaction field is computed with a self-consistent way by having the aid of the electron density of the state of interest (see Figure 3), while in LR-PCM, the excitation energies are determined using a PCM correction dependent on the electron density variation corresponding to the ground to excited state transition. All the QM/PCM and ONIOM calculations are carried out using the Gaussian 09 package.[25]

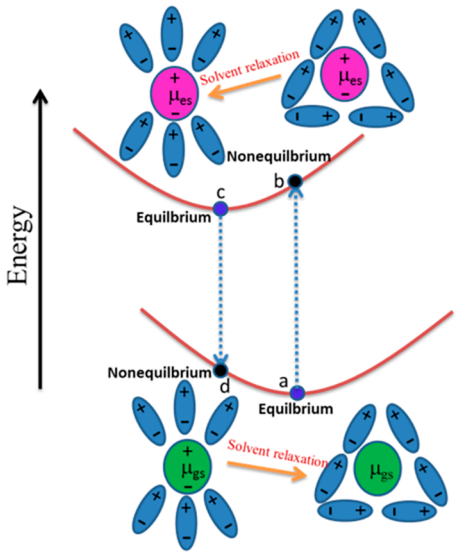

Figure 3. Schematic of interactions of the solute with solvent between Cu(pop)(pz_2BH_2) and a dichloromethane environment with and without solvent reorientation.

2.2. Electronic Structure Calculations. The excited states of the Cu(pop)(pz_2BH_2) molecule are investigated using the TD-DFT for the QM/PCM and ONIOM models. However, the properties of the excited states are strongly dependent on the choice of functional under the framework of TD-DFT for the CT TADF molecule. Thus, the appropriate functional should be determined first. Recently, some ingenious approaches such as the range-separated (RS) exchange density functional method, LC-BLYP, LC-ωPBE, and CAM-B3LYP have been proposed and well applied. In this work, the "optimal tuning" CAM-B3LYP method was used for the solution and solid phases and denoted as CAM-B3LYP*.[26,27] The concept of "'optimal tuning"' corresponds to the optimization of the range-separation parameter ω ($bohr^{-1}$), which was performed by tuning the optDFTw procedure,[28] based on the exact Kohn−Sham (KS) theory, in which the negative HOMO energy for an N-electron system equals to the vertical ionization potential (see formula 1), and the ω optimization results are described in Figure 4. The geometries of S_0 and T_1 states were optimized using the CAM-B3LYP* functional combined with 6-31+G(d) basis set. The S_1 geometries were optimized using the corresponding time-dependent TD-CAM-B3LYP* functional. Harmonic vibrational analyses of these optimized geometries in solution and crystal are performed using the same QM/PCM and ONIOM computational level. These vibrational frequencies and modes are also used in the following the calculation of the TVCF.

$$J^2 = \sum_{i=0}^{1} [\varepsilon_H(N+i) + \mathrm{IP}(N+i)]^2 \tag{1}$$

2.3. Radiative and Nonradiative Rate Constants. Under Fermi's golden rule and the Franck−Condon principle, the radiative rate constant, namely, $k_r(S)$, fluorescence rate and $k_r(T)$, phosphorescence rate, is the integration over the whole emission spectrum, which can be described as the following eqs 2 and 3:[24,29]

$$\sigma_{em}(\omega, T) = \frac{2\omega^3}{3\pi c^3 \hbar^4} |\mu(S_0 \leftarrow T_1/S_1)| \int e^{-i\omega t} e^{i\omega_{S_0 \leftarrow T_1/S_1} t} Z_i^{-1} \rho_{em}(t, T)\, dt \tag{2}$$

$$k_r = \int_0^\infty \sigma_{em}(\omega, T)\, d\omega \tag{3}$$

where, $\rho_{em}(t, T) = \mathrm{Tr}[e^{i\tau_{T_1}} \hat{\hat{H}}_{T_1/S_1} e^{i\tau_{S_0}} \hat{\hat{H}}_{S_0}]$ is the TVCF formula, and $\tau_i = -i\beta - (t/\hbar)$, $\tau_f = t/\hbar$, $\beta = (k_B T)^{-1}$, and $\hat{H}_{T_1/S_1}(\hat{H}_{S_0})$ indicate the harmonic oscillator Hamiltonian of the triplet (singlet) electronic states; $Z_{T_1}^{-1} = \sum_{v=\{0_1, 0_2, \ldots, 0_N\}}^{\infty} e^{-\beta E_v^{T_1}}$ denotes the partition function, where N is the number of normal modes.

Rate constants for intersystem crossing (ISC) processes from initial S_1 state to the final T_1 state could be estimated as eqs 4 and 5.[24,30]

$$k_{ISC} = \frac{2\pi}{\hbar} |\langle T_1|\hat{H}_{SOC}|S_1\rangle|^2 Z_{T_1}^{-1} \sum_{\nu,u} e^{-\beta E_\nu^{T_1}} |\langle \Theta_{T_1,\nu}|\Theta_{S_1,u}\rangle|^2 \delta(E_{T_1,\nu} - E_{S_1,u}) \tag{4}$$

Adopting the Fourier transform of the δ function, eq 4 is rewritten as follows

$$k_{ISC} = \frac{1}{\hbar^2} |\langle T_1|\hat{H}_{SOC}|S_1\rangle|^2 \int_{-\infty}^{\infty} dt\, [e^{i\omega_{T_1,S_1} t} Z_{T_1}^{-1} \rho_{ISC}(t, T)] \tag{5}$$

in which $|\langle T_1|\hat{H}_{SOC}|S_1\rangle|$ is the spin−orbit coupling (SOC) matrix between S_1 and T_1; u and ν indicate the vibrational quantum numbers of the initial S_1 state and the final T_1 state, respectively. The TVCF form is $\rho_{ISC}(t, T) = \mathrm{Tr}[e^{i\tau_{S_1}} \hat{H}_{S1} e^{i\tau_{T_1}} \hat{H}_{T_1}]$, and the delta function δ is to keep the conservation of energy.

DOI: 10.1021/acs.jpca.9b00321
J. Phys. Chem. A 2019, 123, 2080−2090

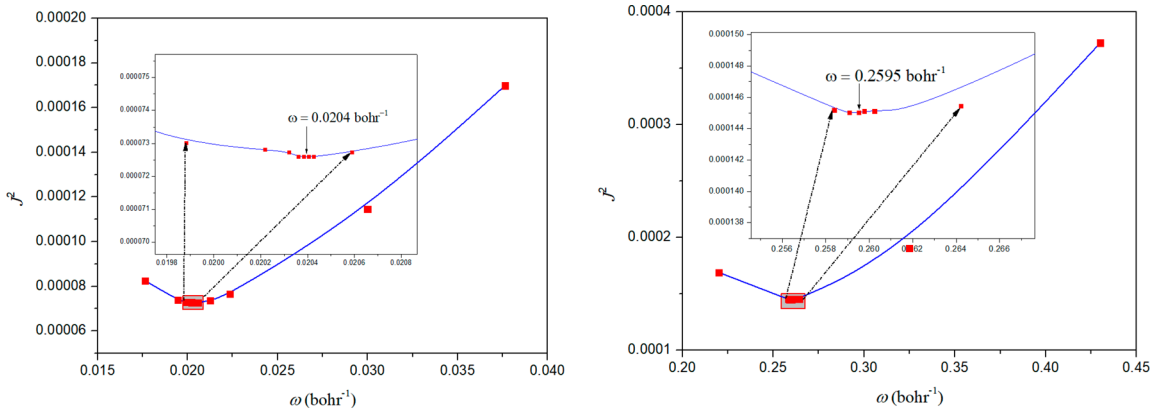

Figure 4. Determining of the optimally tuned range-separation parameter ω (bohr^{-1}) based on eq 2 for the CAM-B3LYP/6-31+G(d) method in the different environments, solution phase (a) and solid phase (b).

Table 1. Comparison of Optimized Vital Structural Parameters with Bond Distances (Å) and Angles (deg) at Equilibrium Geometries of the S_0, S_1, and T_1 States for Cu(pop)(pz_2BH_2) in the Solution and Solid Phases with those of Experimental Crystal Parameters

	CAM-B3LYP* (ω = 0.0204 bohr^{-1}) (PCM)			CAM-B3LYP* (ω = 0.2595 bohr^{-1}) (ONIOM)			expy values[a]
parameters	S_0	S_1	T_1	S_0	S_1	T_1	S_0
R(Cu−P1)	2.2917	2.4332	2.3701	2.2613	2.3434	2.3501	2.2704
R(Cu−P2)	2.2837	2.3997	2.3680	2.2473	2.3073	2.3024	2.2348
R(Cu−N1)	2.0466	2.0058	2.0071	2.0261	2.0117	2.0004	2.0501
R(Cu−N3)	2.0336	1.9970	2.0002	2.0149	1.9941	1.9811	2.0355
∠P1−Cu−P2	112.11	109.09	108.67	112.27	108.23	108.70	112.15
∠N1−Cu−N3	95.52	95.17	95.28	96.94	97.39	96.49	96.14
∠P1−Cu−N1	106.73	100.71	100.91	103.17	101.16	101.11	103.29
∠P2−Cu−N1	119.69	129.41	127.34	120.31	124.91	125.12	121.63

[a]The experimental values are from ref 12.

The rate constant k_{nr} of internal conversion between two electronic states with the same spin state could be derived from the first-order perturbation theory as the following equation

$$k_{nr} = \frac{1}{\hbar^2} R_{kl} \int_{-\infty}^{\infty} dt\ e^{i\omega_{S_1S_0}t} \rho_{S_1S_0}(t, T) \quad (6)$$

where $R_{kl} = \langle \Phi_{S_0} | \hat{P}_{S_1,k} | \Phi_{S_1} \rangle \langle \Phi_{S_1} | \hat{P}_{S_1,l} | \Phi_{S_0} \rangle$ is the nonadiabatic electronic coupling matrix; $\hat{P}_{S_1,k} = -i\hbar\ \partial/\partial Q_{S_1,k}$ represents the normal momentum operator of the kth normal mode in the S_0 state. These detailed derivation and solution of equations could be found in a series of Peng and Shuai reports. The calculations were performed using the TVCF theory, as implemented in the MOMAP 1.0 program package.[24]

Finally, the SOC matrix element was treated as quasi-degenerate perturbation theory using an accurate multicenter spin−orbit mean-field (SOMF) of the Breit−Pauli SOC operator on all atoms.[31] The SOMF method explicitly considers the one- and two-electron parts, and includes the spin-same-orbit as well as spin-other-orbit terms in its two-electron part, which were carried out in the CASSCF level using the ORCA 4.0 program combined with a key word of SOCFlags 1, 3, 3, 1.[32]

3. RESULTS AND DISCUSSION

3.1. Geometric Structures in S_0, S_1, and T_1. The optimally tuned ω values derived for the Cu(pop)(pz_2BH_2) system in the solution and the solid phases are illustrated in Figure 4. As can be seen from Figure 4, in the case of the solution environment with the larger dielectric constants, ε = 8.93, the optimal ω values greatly reduce to the value of 0.0204 bohr^{-1} as compared to the default value of ω = 0.33 bohr^{-1} for CAM-B3LYP. It has long been known that the tuned ω value of a specific system can reflect a 2-fold meaning: (i) the global electron-delocalization degree, in other words, the tuned ω value, is inversely proportional to the spatial extension of the electron-delocalization; (ii) a characteristic distance for exchange switching from short-range DFT-type to long-range exact-exchange (HF-type), that is to say, such a small ω value, implies that there is almost no long-range correction from exact HF exchange. The smaller ω value demonstrates that the electron density in the simulated CH_2Cl_2 environment is more delocalized than that for the isolated molecule in the gas phase. On the contrary, the optimized ω = 0.2595 bohr^{-1} value decreases little relative to the 0.33 bohr^{-1} value for the crystal environment simulated by the ONIOM method. These results indicate that, in order to accurately describe the different polarization environment for the solution and solid states, more DFT-type exchange and less HF exact exchange are contained in the exchange functional. In particular, the precise description of solution phase requires functional to include less "localized" HF exchange and more "delocalized" DFT-type exchange for the Cu(pop)(pz_2BH_2) complex.

DOI: 10.1021/acs.jpca.9b00321
J. Phys. Chem. A 2019, 123, 2080−2090

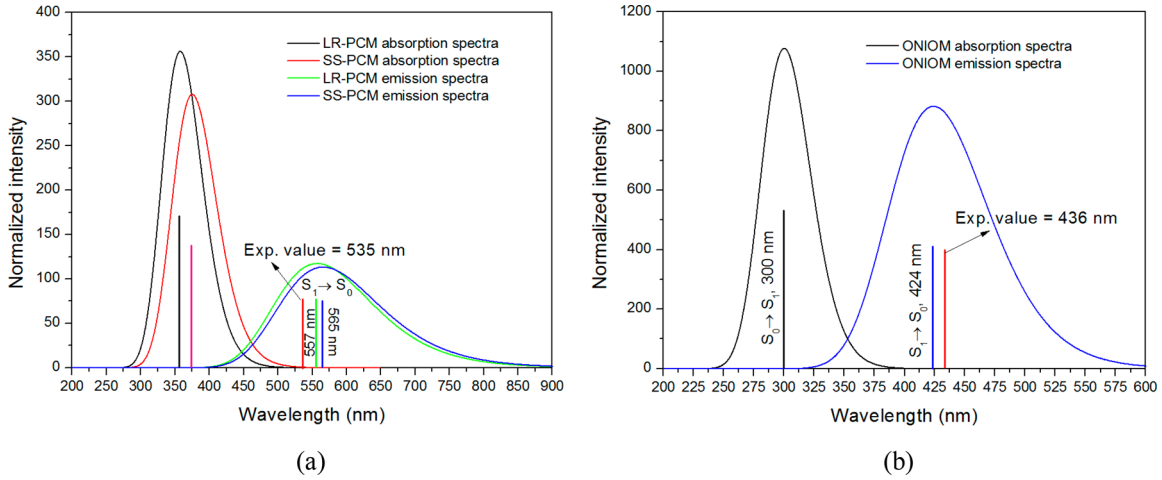

(a) (b)

Figure 5. Simulated absorption and emission spectra of Cu(pop)(pz_2BH_2) at the CAM-B3LYP level: (a) in the CH_2Cl_2 solution (implicit solvation, LR-PCM or SS-PCM) and (b) in the solid state using ONIOM QM/MM method. The experimental spectrum is also listed with red stick lines.

Table 2. Calculated Vertical Absorption Energies (in eV), $E_\perp(S_1)$ and $E_\perp(T_1)$ Relative to the S_0 Minimum, Corresponding Vertical Energy Differences $\Delta E_\perp(S_1\text{-}T_1)$ and Adiabatic Energy Differences $\Delta E(S_1\text{-}T_1)$, and Emission Energies, $E_\perp(S_0)$ at the S_1 Minimum for the Cu(pop)(pz_2BH_2) Complex in the Different Environment Using the Optimally Tuned ω (bohr^{-1}) Range-Separated CAM-B3LYP*/def2-svp (the Default Value of ω = 0.33), with Functional Method and the Experimental Values also Listed

	solution phase (ω = 0.0204)			solid phase (ω = 0.2595)	
states	LR[a]	SS[b]	exptl values[c]	calcd values	exptl values[c]
$E_\perp(S_1)$	3.47 (358 nm)	3.31 (375 nm)	3.35 (370 nm)	4.13 (300 nm)	3.99 (310 nm)
$E_\perp(S_0)$	2.22 (557 nm)	2.19 (565 nm)	2.32 (535 nm)	2.92 (424 nm)	2.84 (436 nm)
$E_\perp(T_1)$	3.29	3.16		3.89	
$\Delta E_\perp(S_1\text{-}T_1)$	0.18 (1452 cm^{-1})	0.15 (1209 cm^{-1})		0.24 (1936 cm^{-1})	0.16 (1300 cm^{-1})
$\Delta E(S_1\text{-}T_1)$	0.11(887 cm^{-1})			0.33 (2662 cm^{-1})	

[a]LR refers to the vertical excitation with linear response solvation. [b]SS is state-specific solvation; and. [c]See reference12.

Table 1 shows the parameters of the optimized geometries in the S_0, S_1, and T_1 states using the optimally tuned functional CAM-B3LYP* in CH_2Cl_2 solution and crystal, respectively, together with the X-ray crystal structure for comparison.[12] In the S_0 state, the central Cu(I) is coordinated by the adjacent P1 and P2 atoms of the diphenylphosphate group and N1 and N3 atoms of the pyrazol group. The corresponding Cu−P1, Cu−P2, Cu−N1, and Cu−N3 bonds are calculated to be lengths of 2.2917 (2.2613), 2.2837 (2.2473), 2.0466 (2.0261), and 2.0336 (2.0049) Å in solution phase (crystal), respectively. Besides this, two vital angles of the ∠P1−Cu−P2 and ∠N1−Cu−N3 are computed to be 112.11° (112.27°), and 95.52° (96.94°) in solution phase (crystal), respectively. The calculated solid phase structure at the S_0 state is in good agreement with the crystal X-ray structure with the largest deviation being less than 1.32° for angles and 0.024 Å for bond lengths, indicating the reliability of the adopted ONIOM approach. By analyzing the structural changes $|\Delta(S_0-S_1$ or $T_1|$ upon excitation, we can find that the Cu−P1 and Cu−P2 bond lengths are elongated compared to those in the S_0 state, whereas the Cu−N1 and Cu−N3 bond are reduced, e.g., the Cu−N1 bond in crystal, from 2.0261 Å in S_0 to 2.0117 Å in S_1 and 2.0004 Å in T_1. The biggest changes of structures occur at the torsional angles ∠P1−Cu−N1 and ∠P2−Cu−N1 from S_0 to S_1 (T_1) states. The torsional angles ∠P1−Cu−N1 and ∠P2−Cu−N1 exhibit great changes of 6.02° (5.82°) and 9.72° (7.69°) in the solution phase, far larger than those in the crystal phase of 2.01° (2.06°) and 4.6° (4.81°) between S_0 and S_1 (T_1) states. These data demonstrate that geometrical modifications are much larger for an isolated molecule in solution than that in crystal cluster upon photoexcitation.

3.2. Excited-State Properties. The pure electronic absorption and emission energies were simulated by performing vertical $S_0 \rightarrow S_1$ and $S_1 \rightarrow S_0$ transitions from the optimized S_0 and S_1 minimum energy structure for Cu(pop)-(pz_2BH_2) in solution and crystal, respectively, as shown in Figure 5 and Table 2; the experimental spectra for comparison are also presented by the red-stick lines. It is clear that our TD-CAM-B3LYP*/PCM and ONIOM (TD-CAM-B3LYP*:UFF) computed spectra match very well with experimental spectra that are measured in solution and crystal. For solution phase, the absorption and emission energies have been computed using both LR-PCM and SS-PCM, the S_0 and S_1 minimum (see Table 2). The experimental emission spectrum is characterized by red line shapes. From the absorption spectrum shown in Figure 5b, which was measured in solid state, a value of approximately 310 nm for the maximum of the first absorption peak can be estimated. The theoretically determined excitation wavelength for $S_0 \rightarrow S_1$ absorption of 300 nm, obtained from the ONIOM (TD-CAM-B3LYP*:UFF) calculation agrees well with the experimental results. And the emission spectrum of crystal is found at a λ_{max} value of 436 nm for the neat sample, coinciding with the calculated value of 424 nm for the S_1 structure in crystalline environment,

DOI: 10.1021/acs.jpca.9b00321
J. Phys. Chem. A 2019, 123, 2080−2090

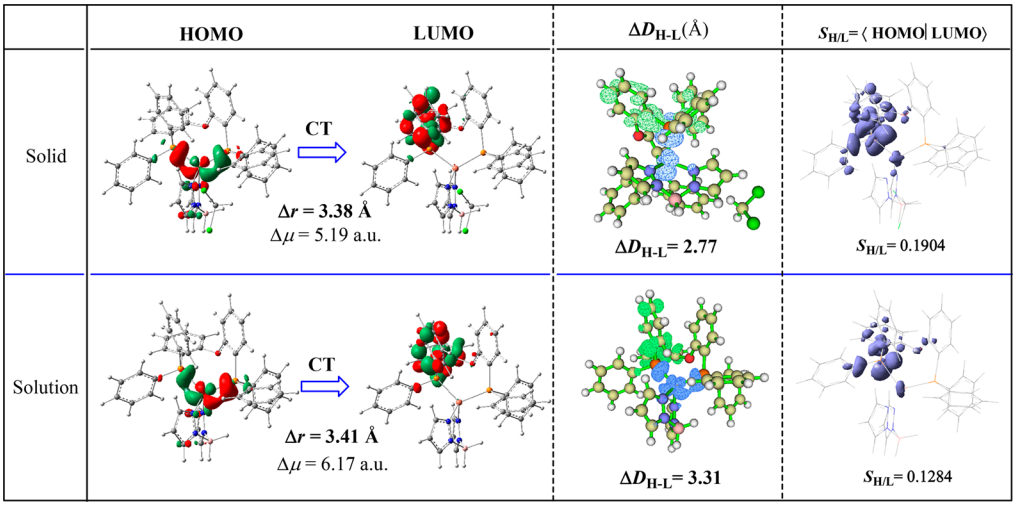

Figure 6. Computed parameters of the charge transfer excited states S_1 of the Cu(pop)(pz_2BH_2) complex at the tuned CAM-B3LYP* theoretical level. Distance between centroid of hole(HOMO) and electron(LUMO), ΔD_{H-L} is given in Å, and the hole−electron overlap integral S_{H-L} is given in au; Δr is the charge transfer distance, and $\Delta\mu$ denotes variation of dipole moment with respect to ground state.

which further confirms the superiority of the QM/MM method in simulating the crystal excited properties.

Concerning to the excited properties of solution phase, it is commonly known that the inclusion of environmental effects is of great importance to estimate the electronic transition properties especially for excited states with a strong CT character. In this work, the CH_2Cl_2 solvent has been employed consistently with experiment. As described in the Computation Details, we have employed two PCM approaches, namely LR-PCM and SS-PCM models for solvation effects, applied in both their equilibrium and nonequilibrium limits. All the values are reported in Table 2; it is worthwhile to highlight that the maximum of an absorption or emission band matches very well with the vertical energies. For instance, the wavelength for $S_0 \rightarrow S_1$ absorption of 375 nm in SS-PCM model matches the experimental value of 370 nm.[12] For the emission processes, it will be accompanied by the nuclear arrangement relaxation of Cu(pop)(pz_2BH_2) as well as solvent CH_2Cl_2 reorganization, but they occur on different time scales. In the SS-PCM model, solvent reorganization has been taken into account in the calculation, namely, the relaxed density matrix of the excited state is used to calculate the solvent reaction field (see Figure 3). The emission energy of 565 nm, obtained from the SS-PCM calculation, is to be very close to the experimental value of 535 nm. Compared with the crystalline environment,[12] solvent reorganization results in a red shift of the emission wavelength from 424 to 565 nm because solvent reorientation is steric hindrance in the solid state. Another noteworthy finding is that the distortion effect, namely, larger configuration change for the S_0 and S_1 minima, leads to breaking of the mirror-image symmetry between absorption and emission in solution (see Figure 5a).

To further explore the charge transfer phenomenon of the excited S_1 states for different environments, some indexes are computed at the tuned CAM-B3LYP* theoretical level, as shown in Figure 6. It can be seen that the excited S_1 states are very similar in nature, and is dominated by the transition from the highest occupied molecular orbital (HOMO) to the lowest unoccupied molecular orbital (LUMO) in both solution and crystal phases. The HOMO has a σ characteristic owing from a linear combination of the Cu(I) 3d orbital and p orbitals of coordinating phosphorus atoms, while the electronic density of LUMO is mainly distributed on the phenylene ring of the pop ligand, as demonstrated a π^* feature. These reveal a special excited state formation: that is a metal−ligand charge-transfer (MLCT) process with the charge transfer from metal Cu(I) to an empty antibonding π^* orbital of the pop ligand.

As stated in the Introduction, the rate of the TADF mechanism becomes high only when the $\Delta E(S_1-T_1)$ is rather small, with the help of thermal energy. To make the $\Delta E(S_1-T_1)$ small enough, thus, the TADF molecule must contain a sufficiently spatially separated HOMO and LUMO because the $\Delta E(S_1-T_1)$ splitting mainly depends on the exchange energy (J, see eqs 7 and 8) in the same orbital configuration of the S_1 and T_1 states.[33]

$$\Delta E(S_1 - T_1) = E(S_1) - E(T_1) = 2J \tag{7}$$

$$J = \iint \phi_H^*(r_1)\phi_L(r_2)(1/r_1 - r_2)\phi_L^*(r_1)\phi_H(r_2)\, dr_1\, dr_2 \tag{8}$$

In eqs 7 and 8, the ϕ_H and ϕ_L correspond to the hole (HOMO) and electron (LUMO) orbitals involved in the excited transition, respectively; The J values are associated with the spatial separation ($r_1 - r_2$, Δr) and overlap integral ($S_{H/L}$) of ϕ_L and ϕ_H at the S_0 state, that is, the larger $S_{H/L}$ of the ϕ_H and ϕ_L and smaller Δr will lead to higher J and $\Delta E(S_1-T_1)$ values.

To achieve the description of the nature of the CT states, the $S_{H/L}$ and Δr of HOMO and LUMO associated with the S_1 transition and ΔD_{H-L}, the length of the hole and electron distribution, as well as $\Delta\mu$, the variation of dipole moment, are all calculated using the Multiwfn program in both solution and the solid state,[34] as inserted in Figure 6. We calculated the charge density differences between the S_1 and S_0 at the S_0 geometries by using $\Delta\rho(r) = \Delta\rho^{ele}(r) - \Delta\rho^{hole}(r)$, and plotted them in the third column of Figure 6, where significant electron density difference are found between the electron donor Cu(I) group with the depletion density (blue) and the pop ligand acceptor with the excess density (red). Thus, the hole and electron on a Cu(pop)(pz_2BH_2) molecule are completely separated, and ΔD_{H-L} values are 3.31 and 2.77 Å, in solution and solid phases, respectively. Another index, denoted as Δr, is based on the charge centroids of the orbitals

DOI: 10.1021/acs.jpca.9b00321
J. Phys. Chem. A 2019, 123, 2080−2090

Table 3. Computed Decay Rate Constants of the S_1 and T_1 States at Different Temperatures by the TVCF Method for the Cu(pop)(pz_2BH_2) Crystal and Solution, with All Units in s^{-1} [a]

temperature (K)	$k_r(S)$	$k_{nr}(S)$	k_{ISC}	k_{RISC}	$k_r(T)$	$k_{ISC}(T_1-S_0)$
ONIOM/CAM-B3LYP* (ω = 0.2595 bohr^{-1}) level						
77	1.58×10^7	–	2.04×10^7	5.77×10^{-4}	3.52×10^4	–
100	1.58×10^7	–	2.38×10^7	1.79×10^{-1}	3.52×10^4	–
150	1.57×10^7	0.55×10^3	2.36×10^7	1.39×10^2	3.61×10^4	2.77×10^2
200	1.57×10^7	0.86×10^3	2.53×10^7	2.19×10^3	3.86×10^4	5.95×10^2
250	1.57×10^7	1.57×10^3	2.73×10^7	1.54×10^4	4.25×10^4	6.28×10^2
300	1.56×10^7	2.98×10^3	2.99×10^7	6.12×10^4	4.75×10^4	6.63×10^2
PCM/CAM-B3LYP* (ω = 0.0204 bohr^{-1}) level						
77	1.53×10^6	–	1.01×10^9	3.95×10^1	8.91×10^3	–
100	1.55×10^6	–	1.18×10^9	1.79×10^2	9.01×10^3	–
150	1.56×10^6	0.95×10^8	1.54×10^9	1.61×10^3	9.08×10^3	5.65×10^2
200	1.59×10^6	1.26×10^8	1.93×10^9	5.78×10^4	9.21×10^3	7.16×10^2
250	1.63×10^6	1.47×10^8	2.35×10^9	5.26×10^5	9.44×10^3	1.05×10^3
300	1.67×10^6	1.68×10^8	2.77×10^9	2.38×10^6	9.71×10^3	1.65×10^3

[a] "–" denotes that rates of intersystem crossing $k_{ISC}(T_1-S_0)$ and $k_{nr}(S)$ tend to be infinitesimal below 100 K.

involved in the transitions and can be demonstrated regarding the hole–electron separation. This larger distance is usually defined having a CT excited nature. But, large distances also mean large TD-DFT errors, relying on the nature of the exchange correlation functional used; therefore, in this paper, the "optimal tuning" range-separation CAM-B3LYP method was used to eliminate TD-DFT errors originating from the long distance CT excitation. According to eqs 7 and 8, $\Delta E(S_1-T_1)$ is an inverse dependence upon Δr and a direct measure of $S_{H/L}$ of the ϕ_H and ϕ_L. The calculated Δr values are of 3.41 and 3.38 Å, respectively, and corresponding to $S_{H/L}$ values are of 0.1284 and 0.1904 in solution and solid phases, which have strong correlation with the $\Delta E(S_1-T_1)$ values of 1209 and 1936 cm^{-1} in the CAM-B3LYP* level, matching the experimental value of 1300 cm^{-1} very well.[35]

3.3. Radiative Rate Constants. The rate constants $k_r(S)$, and $k_r(T)$ are calculated by using the TVCF method considering the displacement, distortion, and Duschinsky rotation effects between different electronic states, as shown in Table 3. The $k_r(S)$, and $k_r(T)$ correspond to the fluorescence and phosphorescence emissions from both S_1 and T_1 states, respectively. Fluorescence rates $k_r(S)$ are calculated to be $(1.58-1.56) \times 10^7$ s^{-1} (τ = 63.3 ns) in the crystal phase, from 77 to 300 K, which are almost independent of the temperature; they match very well with the experimental value of 30 ns.[12] In line with the simple Einstein spontaneous emission formula $k_r = f\Delta E^2/1.449$, the radiative rates are primarily controlled by the oscillator strength (f) and the excitation energy (ΔE). From Table 3, the radiative rates increase from solution ($(1.53-1.67) \times 10^6$ s^{-1} in CH_2Cl_2) to crystal by about 10 times. This is mainly attributed to the larger electric transition dipole moment, which in turn depends upon the greater degree of intramolecular conjugation in the aggregation crystal state.

In terms of phosphorescence $k_r(T)$, actually, the direct electric transition dipole moment of the $T_1 \rightarrow S_0$ emission is strictly spin-forbidden in the regime of an unrelativistic treatment. However, compared to the organic molecule, the heavy element effect of the metal atom can cause the significant SOC interaction between different spin states (triplet and singlet) in the organometallic complexes, which leads to nonzero probability of the $T_1 \rightarrow S_0$ emission because of borrowing from the transition moment of spin-allowed electronic transitions, namely, from $T_m \leftrightarrow T_1$ or $S_n \leftrightarrow S_0$ moment, as indicated in eq 9:[35]

$$\mu(S_0 \leftarrow T_{1,\varsigma}) = \sum_{n\in\text{singlets}} \frac{\langle S_0|\mu_\alpha|S_n\rangle\langle S_n|\hat{H}_{SOC}|T_{1,\varsigma}\rangle}{E(T_{1,\varsigma}) - E(S_n)} + \sum_{m\in\text{triplets}} \sum_{\varsigma=-1,0,1} \frac{\langle T_{1,\varsigma}|\mu_\alpha|T_m\rangle\langle T_m|\hat{H}_{SOC}|S_0\rangle}{E(T_m) - E(S_0)} \quad (9)$$

Here $T_{1,\varsigma}$ denotes the ζ (= −1, 0, and +1) spin sublevel of triplet T_1 state being subject to the zero-field splitting (ZFS) induced by internal magnetic perturbations, and $\hat{H}_{SOC}$ is the SOC operator.

As we all know that the larger ZFS substates of the T_1 state have quite different radiative and nonradiative properties. However, for the Cu(I) complex, the ΔE(ZFS) value, representing the energy separation between the T_{-1} and T_{+1} substates, is expected to be significantly small owing to the smaller SOC constant of Cu (857 cm^{-1}) than that of Ir 1150 cm^{-1} atom. Recently, Yersin and co-workers[12] have experimentally determined to ZFS values of the order of 1 to 10 cm^{-1} for a series of Cu(I) complexes. Our theoretical calculation shows that $\Delta E_{-1,0}$ = 0.1 cm^{-1} and $\Delta E_{0,+1}$ = 4.7 cm^{-1}, in good agreement with experiment at the T_1 geometryl see Table S1 in Supporting Information. Thus, we merely compute the phosphorescence rates $k_r(T)$ that are averaged over the three triplet substates, $T_{-1,0,+1}$ using the TVCF method. In the temperature range of 77 to 300 K, the $k_r(T)$ values are estimated to be $(8.91-9.71) \times 10^3$ s^{-1} in CH_2Cl_2 and $(3.52-4.75) \times 10^4$ s^{-1} in crystal phase, respectively, see Table 3. In contrast, the $k_r(T)$ of crystal is about 1 order of magnitude larger than that for the solution, which is mainly due to the larger transition dipole moment, $\langle S_0|\mu_\alpha|S_n\rangle$ of the spin-allowed singlet states in crystal based on eq 9 (the second term is often negligible because $E(T_m) - E(S_0)$ is relatively very large).

3.4. Internal Conversion Rate Constants. As far as the processes of the $S_1 \rightarrow S_0$ internal conversion are concerned, Table 3 reveals that the $k_{nr}(S)$ in the solution phase is approximately 5 orders of magnitude larger than that in the crystal phase because the distorted motions of low frequency

DOI: 10.1021/acs.jpca.9b00321
J. Phys. Chem. A 2019, 123, 2080–2090

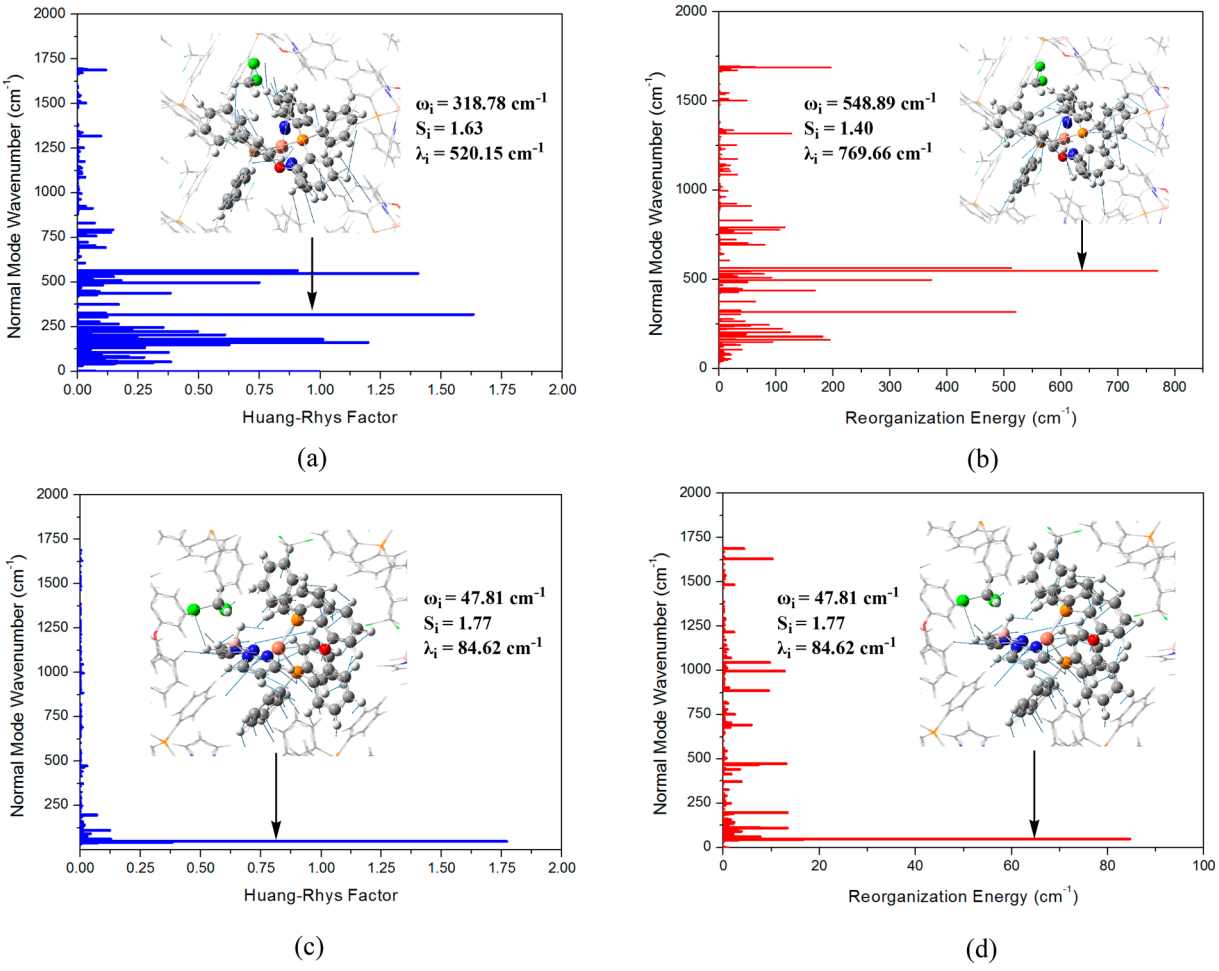

Figure 7. Calculated Huang–Rhys factors and Reorganization energies versus the normal-mode frequencies of Cu(pop)(pz_2BH_2)(CH_2Cl_2) molecule in the solid phase for energy conversion between S_1 and S_0 (a, b) and between S_1 and T_1 (c, d), as well as the displacement vectors of three important vibration modes are depicted.

normal modes are largely restrained for the AIE molecules in the crystal, moreover, we also note that the $k_{nr}(S)$ values increase gradually with increasing temperature from 77 to 300 K in the solution and crystal phases. To further explore the suppressed nonradiative channel in aggregates, here, elaborating the intramolecular reorganization energy or relaxation energy is the most appropriate. Under the harmonic oscillator approximation, the intramolecular reorganization energy, λ_k, can be expressed as a summation over all vibrational normal modes i, as following:[36]

$$\lambda_k = \sum \lambda_i = \sum \hbar\omega_i S_i;\ S_i = \frac{\omega_i D_i^2}{2\hbar} \qquad (10)$$

In eq 10, ω_i and S_i denote the frequency and Huang–Rhys factor of the ith normal mode, and D_i is the displacement along the ith normal mode coordinate between the equilibrium position of two electronic states k, respectively. The S_i and λ_k of each normal mode are useful parameters estimating the extent of electron-vibration coupling between different states.

The S_i and λ_k of the crystal phase for the S_1 and S_0 states are depicted in parts a and b of Figure 7, and those for the solution phase Figure S2 in Supporting Information. Figure 8 also shows comparison of the S_i factors for the solid and solution phases from the $S_1 \rightarrow S_0$ internal conversion process. It can be seen that the S_i factors of Cu(pop)(pz_2BH_2) are much smaller

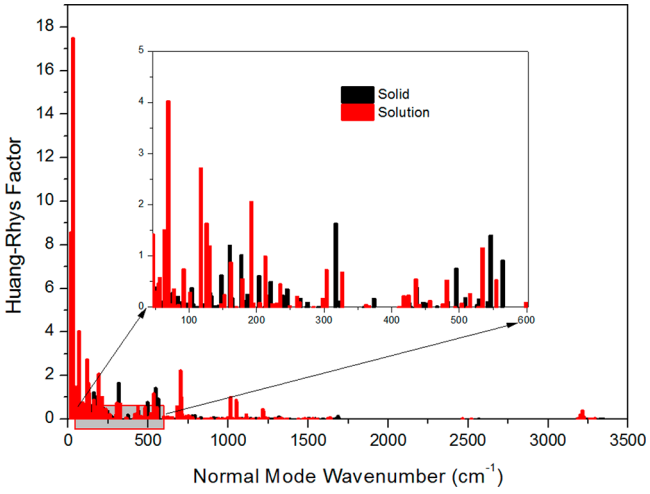

Figure 8. Comparison of Huang–Rhys factors for the solid phase (red stick lines) and the solution phase (black stick lines) from the $S_1 \rightarrow S_0$ internal conversion processes.

in the crystal than in the solution, particularly for the low frequency region of <600 cm^{-1}. These also reveal that the low frequency vibrations are restrained in the crystal phase, and vibration modes having large S_i factors all present in the low

DOI: 10.1021/acs.jpca.9b00321
J. Phys. Chem. A 2019, 123, 2080–2090

frequency region, such as ω_i = 162.17 cm^{-1}, S_i = 1.2, λ_i = 184.23 cm^{-1}; ω_i = 318.78 cm^{-1}, S_i = 1.6, λ_i = 520.15 cm^{-1}; and ω_i = 548.89 cm^{-1}, S_i = 1.41, λ_i = 769.66 cm^{-1} in the crystal. These low frequency vibration modes are assigned as the rotational motion of the phenylene ring in the pop ligand, which indicates the importance of low frequency modes couplings in the nonradiative $S_1 \rightarrow S_0$ decay. It is clear that the vibrational modes with large λ_i are regarded as significant pathways to nonradiatively dissipate the excited state energies. In contrast, the energy dissipation pathways are easily quenched via low frequency components in the solution phase, resulting in the high $k_{nr}(S)$. Such features are supported by the geometrical modifications from S_1 to S_0 states (see Figure 9). These results reflect that aggregation turns "on or off" the fluorescence emission by controlling the nonradiative energy dissipation channel of low frequency.

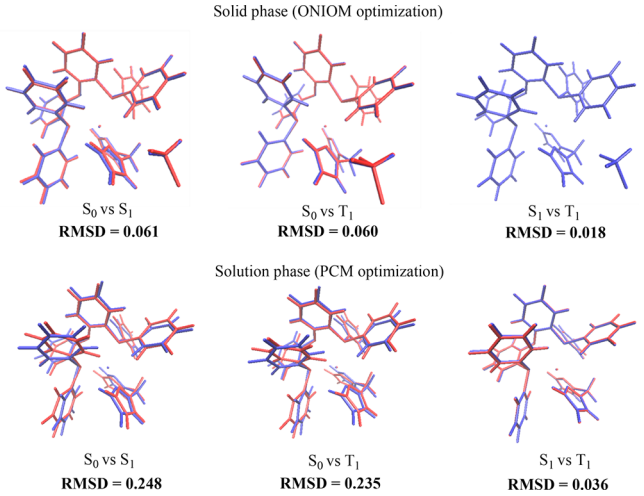

Figure 9. Comparison of superimposed ONIOM/PCM optimized structures of the S_0, S_1, and T_1 states. RMSD = root mean square displacement/deviation.

3.5. Intersystem Crossing and Fluorescence Quantum Efficiency. As mentioned above, TADF can in principal effectively take place, which can be achieved with the help of the effective RISC process. Namely, the S_1 state has to be repopulated with any temperature increase. This means that the RISC rates have to be larger than the rates of radiative and nonradiative decay of the T_1 state to the ground state. In particular, the RISC rates from T_1 to S_1 should be larger than the phosphorescence rates $k_r(T)$ because the ISC process from the T_1 to S_0 states are very slow owing to the huge energy gap between the T_1 and S_0 states in our studied systems. Here, ISC and RISC rates taking the vibrational contributions into account were computed according to eqs 4 and 5 by applying the MOMAP 1.0 program,[24,37,38] as shown in Table 3. For the solution phase, it is found that the RISC rate k_{RISC} is 2.38 × 10^6 s^{-1} at the temperature of 300 K, which is about 3 order of magnitude larger than the mean phosphorescence rate $k_r(T)$, 9.71 × 10^3 s^{-1}, and ISC rate $k_{ISC}(T_1-S_0)$ of 1.65 × 10^3 s^{-1} from the T_1 to S_0 states. But, the fluorescence rate $k_r(S)$ = 1.67 × 10^6 s^{-1} seems to be much smaller as compared with the ISC rate of 2.77 × 10^9 s^{-1}, at the same time, having the huge large nonradiative rate $k_{nr}(S)$ of 1.68 × 10^8 s^{-1}. These will cause the issue that the S_1 state populations can not be rapidly equilibrated after decaying radiatively at the room temperature, and delayed fluorescence is unlikely to occur.

For the crystal phase, the ISC and RISC rates are all smaller than those in solution phase. In order to further understand the variation of the ISC and RISC rates from solution phase to crystal, we have calculated the S_i and λ_i of vibrational modes with significant contributions. It can be seen from Figure 7, parts c and d, that the low frequency normal modes associated with the twisting motions of the phenylene ring in the pop ligand and the pz_2BH_2 groups are mainly responsible for these ISC and RISC processes between S_1 and T_1. These low frequency modes have much smaller S_i factors in crystal than those in the solution phase; therefore, the related ISC and RISC process in the crystal are inhibited intensively (see Figure 9). The ISC and RISC rates are calculated to be 2.99 × 10^7 s^{-1} and 6.12 × 10^4 s^{-1} in the crystal, which are smaller than 2.77 × 10^9 s^{-1} and 2.38 × 10^6 s^{-1} in solution at 300 K. In addition, it is worthwhile mentioning that 2.99 × 10^7 s^{-1} > 1.56 × 10^7 s^{-1} + 2.98 × 10^3 s^{-1}, and 6.12 × 10^4 > 4.75 × 10^4 s^{-1} + 6.63 × 10^2 s^{-1} are suitable for this $k_{ISC} > k_r(S) + k_{nr}(S)$ and $k_{RISC} > k_r(T) + k_{ISC}(T_1-S_0)$ conditions in crystal at 300 K (see Table 3 and Figure 10);[39] therefore, we conclude that the S_1 state can redistribute originating from the T_1 state at room temperature, so the delayed fluorescence possibly thus occurs.

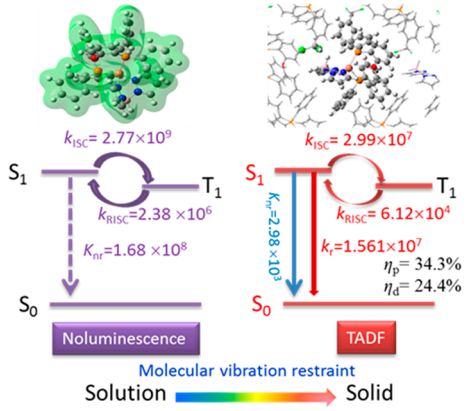

Figure 10. Relationship diagram between molecular vibration suppression and luminescence properties from solution phase to solid phase. Related kinetic decay rate constants are also illustrated at room temperature 300 K.

The prompt and delayed fluorescence quantum efficiency η_p and η_d from the S_1 state to the ground state can be calculated by eq 11, respectively, at 300 K.[40]

$$\eta_p = k_r/(k_r(S) + k_{nr}(S) + k_{ISC}) \text{ and } \eta_d = \sum_{m=1}^{\infty} (\eta_{ISC}\eta_{RISC})^m \eta_p \quad (11)$$

where $\eta_{ISC} = k_{ISC}/(k_r(S) + k_{nr}(S) + k_{ISC})$ and $\eta_{RISC} = k_{RISC}/(k_r(T) + k_{nr}(T_1\text{-}S_0) + k_{RISC})$.

The calculated results are shown in Figure 10. The results corresponding to the η_p and η_d are 34.3 and 24.4%, respectively, and the total photoluminescent efficiency is 58.7%, which is good agreement with the experimental value of 45 ± 5% observed in solid state. For the solution phase, the photoluminescent efficiency tends to zero, which is because the energy dissipation pathways are easily quenched via low frequency components (supported by the larger geometrical

DOI: 10.1021/acs.jpca.9b00321
J. Phys. Chem. A 2019, 123, 2080−2090

modifications from S_1 to S0 states, see Figure 9) in the solution phase, resulting in the high $k_{nr}(S)$. The results show that the photoluminescent efficiency of aggregation-induced emission for Cu(pop)(pz_2BH_2) in the crystal state is far larger than that in the solution state.

4. CONCLUSION

We comparatively investigated the electronic structures and the photophysical processes for Cu(pop)(pz_2BH_2) between the solution phase (CH_2Cl_2) and the crystal phase, using the TVCF theory combined with the PCM and ONIOM model methods. For the accurate prediction of photophysical properties for TADF molecules, the optimally tuned range-separated hybrid functional (CAM-B3LYP*) with the PCM and ONIOM models is also adopted in this study. The results demonstrate that the technique of the optimally tuned range-separated hybrid functional gives an outstanding description for charge transfer excited state properties and matches excellent agreement with experimental values.

The calculated solid phase structure at the S_0 state is in good agreement with the crystal X-ray structure with the largest deviation being less than 1.32° for angles and 0.024 Å for bond lengths, indicating the reliability of the adopted ONIOM approach. For the nonradiative processes of the $S_1 \rightarrow S_0$ internal conversion, the energy dissipation is easily quenched via low frequency components having a large λ_i in the solution phase, resulting in high $k_{nr}(S)$. These low frequency vibration modes mainly originate from the rotational motion of the phenylene ring in the pop ligand, which are easily hindered through intermolecular interactions in the aggregated state (crystal phase), and $k_{nr}(S)$ is predicted to be decreased by about 5 orders of magnitude upon aggregation. As to the ISC and RISC between the S_1 and T_1 states, the low frequency vibrational modes associated with the twisting motions of the phenylene ring in the pop ligand and the pz_2BH_2 groups are mainly responsible for the efficient ISC and RISC processes. The corresponding S_i is suppressed in the crystal compared to in solution phase owing to the rigidity surroundings, which leads to ISC and RISC reduced in crystal compared with that in solution. In addition, an enhanced fluorescence efficiency of 58.7% is found in the crystal phase compared with in solution phase (≈0), which reflects the AIE mechanism. But, at low temperature $T < 100$ K, the RISC rate is sharply changed, $k_{RISC} \ll k_r(T)$ or k_{ISC}, which cannot induce an occurrence of delayed fluorescence. The comparison results show that environmental effects are very important for the regulation of photophysical processes of the Cu(I) complexes. Our investigation provides valuable information on the TADF mechanism for the Cu(I) compounds, which would be helpful for designing novel excellent TADF materials.

■ ASSOCIATED CONTENT

Supporting Information

The Supporting Information is available free of charge on the ACS Publications website at DOI: 10.1021/acs.jpca.9b00321.

Illustrative picture for constructing the ONIOM QM/MM model of crystal Cu(pop)(pz_2BH_2); calculated Huang−Rhys factors and reorganization energies versus the normal-mode frequencies of Cu(pop)(pz_2BH_2) molecule in the solution and crystal phase; comparison of superimposed ONIOM/PCM optimized structures of the S_0, S_1, and T_1 states; computed vertical transition energies ΔE, oscillator strength f, radiative rates k_r, and lifetimes τ of the spin sublevels at the T_1 minimum; and calculated spin−orbit coupling matrix constants (SOCC) (cm^{-1}) between T_1 and S_1 for the Cu(pop)-(pz_2BH_2) complex (PDF)

■ AUTHOR INFORMATION

Corresponding Author

*E-mail: lvling002@163.com.

ORCID

Lingling Lv: 0000-0001-6208-6629

Notes

The authors declare no competing financial interest.

■ ACKNOWLEDGMENTS

The authors gratefully acknowledge financial support from the National Natural Science Foundation of China (Grant No. 21263022, 21663025, 21663024). We gratefully thank Dr. Haitao Sun (East China Normal Universty) for providing the help in using the PCM-tuned CAM-B3LYP* approach.

■ REFERENCES

(1) Yang, Z. Y.; Mao, Z.; Xie, Z. L.; Zhang, Y.; Liu, S. W.; Zhao, J.; Xu, J. R.; Chi, Z. G.; Aldred, M. P. Recent advances in organic thermally activated delayed fluorescence materials. *Chem. Soc. Rev.* **2017**, *46*, 915−1016.

(2) Tao, Y.; Yuan, K.; Chen, T.; Xu, P.; Li, H. H.; Chen, R. F.; Zheng, C.; Zhang, L.; Huang, W. Thermally Activated Delayed Fluorescence Materials Towards the Breakthrough of Organoelectronics. *Adv. Mater.* **2014**, *26*, 7931−7958.

(3) Komino, T.; Tanaka, H.; Adachi, C. Selectively controlled orientational order in linear-shaped thermally activated delayed fluorescent dopants. *Chem. Mater.* **2014**, *26*, 3665−3671.

(4) Uoyama, H.; Goushi, K.; Shizu, K.; Nomura, H.; Adachi, C. Highly efficient organic light-emitting diodes from delayed fluorescence. *Nature* **2012**, *492*, 234−238.

(5) Adachi, C.; Baldo, M. A.; Thompson, M. E.; Forrest, S. R. Nearly 100% internal phosphorescence efficiency in an organic light-emitting device. *J. Appl. Phys.* **2001**, *90*, 5048−505.

(6) Zhao, B.; Zhang, T.; Chu, B.; Li, W.; Su, Z.; Luo, Y.; Li, R.; Yan, X.; Jin, F.; Gao, Y.; et al. Highly efficient tandem full exciplex orange and warm white OLEDs based on thermally activated delayed fluorescence mechanism. *Org. Electron.* **2015**, *17*, 15−21.

(7) Czerwieniec, R.; Leitl, M. J.; Homeier, H. H. H.; Yersin, H. Cu(I) complexex-Thermally activated delayed fluorescence. Photophysical approach and material design. *Coord. Chem. Rev.* **2016**, *325*, 2−28.

(8) Leitl, M. J.; Krylova, V. A.; Djurovich, P. I.; Thompson, M. E.; Yersin, H. Phosphorescence versus thermally activated delayed fluorescence. Controlling singlet−triplet splitting in brightly emitting and sublimable Cu(I) compounds. *J. Am. Chem. Soc.* **2014**, *136*, 16032−16038.

(9) Dumur, F. Recent advances in organic light-emitting devices comprising copper complexes: A realistic approach for low-cost and highly emissive devices? *Org. Electron.* **2015**, *21*, 27−39.

(10) Hofbeck, T.; Monkowius, U.; Yersin, H. Highly Efficient luminescence of Cu(I) compounds: thermally activated delayed fluorescence combined with short-lived phosphorescence. *J. Am. Chem. Soc.* **2015**, *137*, 399−404.

(11) Li, G.; Nobuyasu, R.; Zhang, B. H.; Geng, Y.; Yao, B.; Xie, Z. Y.; Zhu, D. X.; Shan, G. G.; Che, W. L.; Yan, L. K.; Su, Z. M.; Dias, F.; Robert Bryce, M.; et al. Thermally activated delayed fluorescence in Cu(I) complexes originating from restricted molecular vibrations. *Chem. - Eur. J.* **2017**, *23*, 11761−11766.

(12) Czerwieniec, R.; Yu, J.; Yersin, H. Blue-light Emission of Cu(I) complexes and singlet harvesting. *Inorg. Chem.* **2011**, *50*, 8293−8301.

DOI: 10.1021/acs.jpca.9b00321
J. Phys. Chem. A 2019, 123, 2080−2090

(13) Chen, Y.; Lam, J. W. Y.; Kwok, R. T. K.; Liu, B.; Tang, B. Z. Aggregation-induced emission: fundamental understanding and future developments. *Mater. Horiz.* **2019**, DOI: 10.1039/C8MH01331D.
(14) Gao, Y.; Chen, W.-K.; Wang, Z.-R.; Fang, W.-H.; Cui, G. L. QM and ONIOM studies on thermally activated delayed fluorescence of copper(I) complexes in gas phase, solution, and crystal. *Phys. Chem. Chem. Phys.* **2018**, *20*, 24955−24967.
(15) Lv, L. L.; Yuan, K.; Wang, Y. C. Theoretical studying of basic photophysical processes in a thermally activated delayed fluorescence copper(I) complex: Determination of reverse intersystem crossing and radiative rate contants. *Org. Electron.* **2018**, *52*, 110−122.
(16) Lv, L. L.; Yuan, K.; Wang, Y. C. Basic photophysical analysis of a thermally activated delayed fluorescence copper(I) complex in solid state: theoretical estimations from a polarizable continuum model (PCM)-tuned range-separated density functional approach. *Phys. Chem. Chem. Phys.* **2018**, *20*, 6548−6561.
(17) Sun, H. T.; Zhong, C.; Brédas, J.-L. Reliable prediction with tuned range-separated functionals of the singlet−triplet gap in organic emitters for thermally activated delayed fluorescence. *J. Chem. Theory Comput.* **2015**, *11*, 3851−3858.
(18) Sun, H. T.; Hu, Z. B.; Zhong, C.; Chen, X. K.; Sun, Z. R.; Brédas, J.-L. Impact of dielectric constant on the singlet−triplet gap in thermally activated delayed fluorescence materials. *J. Phys. Chem. Lett.* **2017**, *8*, 2393−2398.
(19) Körzdörfer, T.; Brédas, J. L. Organic electronic materials: recent advances in the DFT description of the ground and excited states using tuned range-separated hybrid functionals. *Acc. Chem. Res.* **2014**, *47*, 3284−91.
(20) Lv, L. L.; Liu, K.; Yuan, K.; Zhu, Y. C.; Wang, Y. C. Thermally activated delayed fluorescence processes for Cu(I) complexes in solid-state: a computational study using quantitative prediction. *RSC Adv.* **2018**, *8*, 28421−28432.
(21) Huang, S.; Zhang, Q.; Shiota, Y.; Nakagawa, T.; Kuwabara, K.; Yoshizawa, K.; Adachi, C. Computational prediction for singlet- and triplet-transition energies of charge-transfer compounds. *J. Chem. Theory Comput.* **2013**, *9*, 3872−3877.
(22) Sun, H. T.; Ryno, S.; Zhong, C.; Ravva, M. K.; Sun, Z. R.; Körzdörfer, T.; Brédas, J.-L. Ionization energies, electron affinities, and polarization energies of organic molecular crystals: quantitative estimations from a polarizable continuum Model (PCM)-tuned range-separated density functional approach. *J. Chem. Theory Comput.* **2016**, *12*, 2906−2916.
(23) Chung, L. W.; Sameera, W. M. C.; Ramozzi, R.; Page, A. J.; Hatanaka, M.; Petrova, G. P.; Harris, T. V.; Li, X.; Ke, Z. F.; Liu, F.; Li, H.-B.; Ding, L.; Morokuma, K. The ONIOM method and its applications. *Chem. Rev.* **2015**, *115*, 5678−5796.
(24) Niu, Y. L.; Li, W. Q.; Peng, Q.; Geng, H.; Yi, Y. P.; Wang, L. J.; Nan, G. J.; Wang, D.; Shuai, Z. G. MOlecular MAterials Property Prediction Package (MOMAP) 1.0: a software package for predicting the luminescent properties and mobility of organic functional materials. *Mol. Phys.* **2018**, *116*, 1078−1090.
(25) Frisch, M. J.; Trucks, G. W.; Schlegel, H. B., et al. *Gaussian 09*, Revision-D.01; Gaussian Inc.: Wallingford, CT, 2009.
(26) Yanai, T.; Tew, D.; Handy, N. A new hybrid exchange-correlation functional using the Coulomb-attenuating method (CAM-B3LYP). *Chem. Phys. Lett.* **2004**, *393*, 51−57.
(27) Chai, J. D.; Head-Gordon, M. Systematic optimization of long-range corrected hybrid density functionals. *J. Chem. Phys.* **2008**, *128*, 084106.
(28) Lu, T. optDFTw and scanDFTw program v1.0. http://sobereva.com/346 (2017.3.8).
(29) Niu, Y. L.; Peng, Q.; Deng, C. M.; Gao, X.; Shuai, Z. G. Theory of excited state decays and optical spectra: Application to polyatomic molecules. *J. Phys. Chem. A* **2010**, *114*, 7817−7831.
(30) Peng, Q.; Niu, Y. L.; Shi, Q.; Gao, X.; Shuai, Z. G. Correlation function formalism for triplet excited state decay: combined spin-orbit and nonadiabatic couplings. *J. Chem. Theory Comput.* **2013**, *9*, 1132−1143.
(31) Neese, F. Efficient and accurate approximations to the molecular spin-orbit coupling operator and their use in molecular g-tensor calculations. *J. Chem. Phys.* **2005**, *122*, 034107.
(32) Neese, F. The ORCA program system, WIREs Comput. *Mol. Sci.* **2012**, *2*, 73−78.
(33) Chen, T.; Zheng, L.; Yuan, J.; An, Z. F.; Chen, R. F.; Tao, Y.; Li, H. H.; Xie, X. J.; Huang, W. Understanding of the control of singlet-triplet splitting for organic exciton manipulating: A combined theoretical and experimental approach. *Sci. Rep.* **2015**, *5*, 10923.
(34) Lu, T.; Chen, F. Multiwfn: a multifunctional wavefunction analyzer. *J. Comput. Chem.* **2012**, *33*, 580−592.
(35) Baryshnikov, G.; Minaev, B.; Ågren, H. Theory and calculation of the phosphorescence Phenomenon. *Chem. Rev.* **2017**, *117*, 6500−6537.
(36) Samanta, P. K.; Kim, D.; Coropceanu, V.; Brédas, J.-L. Up-conversion intersystem crossing rates in organic emitters for thermally activated delayed fluorescence: Impact of the nature of singlet vs triplet excited states. *J. Am. Chem. Soc.* **2017**, *139*, 4042−4051.
(37) Gibson, J.; Monkman, A. P.; Penfold, T. J. The importance of vibronic coupling for efficient reverse intersystem crossing in thermally activated delayed fluorescence molecules. *ChemPhysChem* **2016**, *17*, 2956−2961.
(38) Penfold, T. J.; Gindensperger, E.; Daniel, C.; Marian, C. M. Spin-vibronic mechanism for intersystem crossing. *Chem. Rev.* **2018**, *118*, 6975−7025.
(39) Föller, J.; Kleinschmidt, M.; Marian, C. M. Phosphorescence or thermally activated delayed fluorescence? Intersystem crossing and radiative rate constants of a three-coordinate copper(I) complex determined by quantum-chemical methods. *Inorg. Chem.* **2016**, *55*, 7508−7516.
(40) Peng, Q.; Fan, D.; Duan, R. H.; Yi, Y. P.; Niu, Y. L.; Wang, D.; Shuai, Z. G. Theoretical study of conversion and decay processes of excited triplet and singlet states in a thermally activated delayed fluorescence molecule. *J. Phys. Chem. C* **2017**, *121*, 13448−13456.

DOI: 10.1021/acs.jpca.9b00321
J. Phys. Chem. A 2019, 123, 2080−2090